


Bulk generalized Dzyaloshinskii-Moriya interaction in \mathcal{PT} -symmetric antiferromagnetsFarzad Mahfouzi^{*} and Nicholas Kioussis[†]*Department of Physics and Astronomy, California State University, Northridge, California 91330, USA* (Received 28 March 2022; revised 29 July 2022; accepted 2 December 2022; published 15 December 2022)

The Dzyaloshinskii-Moriya interaction (DMI) in magnetic materials plays an important role in spintronics, giving rise to chiral spin textures such as the nucleation and propagation of domain walls and skyrmions. The necessary ingredient for the emergence of the DMI is the lack of inversion symmetry combined with elements with strong spin-orbit coupling. We report on a first-principles investigation of generalized DMIs in bulk centrosymmetric crystals with noncentrosymmetric local sublattices, where we consider a prototype family of \mathcal{PT} -symmetric antiferromagnets, including, Mn_2Au , MnPd_2 and MnCuAs in the tetragonal and orthorhombic phases. We employ a Green's function approach to calculate the interatomic relativistic exchange coupling which can, in turn, determine the *sublattice* elements of the generalized fifth-order DMI tensor $D_{\alpha\beta,\gamma}^{ss'}$. We demonstrate that the breaking of the local mirror symmetry and the resulting local Rashba-type spin-momentum locking yield local DMIs with opposite signs on the two antiparallel sublattices. We present numerical results and provide analytical expressions for the magnon dispersion in the presence of the sublattice DMI and show that the intra- (inter-) sublattice DMIs result in identical (opposite) contributions to the nonreciprocal components of the two low-frequency antiferromagnetic magnon modes.

DOI: [10.1103/PhysRevB.106.L220404](https://doi.org/10.1103/PhysRevB.106.L220404)

Antiferromagnetic (AFM) materials have attracted a lot of attention as potential candidates for active elements in spintronic devices due to their weak sensitivity to magnetic field perturbations, potential for miniaturization, and ultrafast switching in the terahertz (THz) frequency range [1–5]. The current-induced antidamping- and fieldlike spin-orbit torque (SOT) has been employed to control and switch the Néel vector in the two prototypical bulk centrosymmetric metallic Mn_2Au [6–8] and Dirac semimetal MnCuAs [9] antiferromagnets, thus demonstrating a viable approach to AFM-based memories and providing a route to ultrafast spintronic devices. On the other hand, the Néel vector can be detected using the anisotropic magnetoresistance effect [1,4,9], optical methods [10–12], the anomalous Hall effect in noncollinear antiferromagnets such as Mn_3X ($X = \text{Ge}, \text{Sn}, \text{Ga}, \text{Ir}$) [13–15], and the anisotropic spin Hall effect [16–18]. Another intriguing topological antiferromagnet is the Dirac nodal line semimetal MnPd_2 in which reorientation of the Néel vector leads to switching between the symmetry-protected degenerate state and the gapped state associated with the dispersive Dirac nodal line at the Fermi energy [18].

The AFM ordering in Mn_2Au , CuMnAs , and MnPd_2 breaks both the time-reversal symmetry \mathcal{T} and the space inversion symmetry \mathcal{P} but preserves the \mathcal{PT} product [6,9,18]. The breaking of the local space inversion on each sublattice layer can be readily seen from Fig. 1(a), where, e.g., the spin-up Mn layers are sandwiched between Au and spin-down Mn layers. This results in the presence of Rashba-type spin-momentum locking with opposite chirality [19–24] on the two

magnetic Mn sublattices, which can, in turn, be employed to induce Néel SOT and reorient the direction of the AFM ordering [6,7,25]. Furthermore, *ab initio* calculations revealed the emergence of toroidal moments [26] in the Mn_2Au and CuMnAs antiferromagnets and showed that their experimentally reported SOT behaviors are consistent with the final states aligning their toroidal moments parallel to the applied electric current [26,27].

The Dzyaloshinskii-Moriya interaction (DMI) [28,29] emerges in magnetic systems with artificially or intrinsically broken inversion symmetry. This relativistic antisymmetric exchange interaction results from the strong spin-orbit coupling (SOC) and often favors noncollinear magnetic states, thus leading to the formation of spin spirals or topologically nontrivial spin structures such as skyrmions [30–32]. In addition, the DMI results in a nonreciprocal dispersion for long-wavelength spin waves [33], $\omega_{\vec{q}} = \sum_{\alpha\beta} D_{\alpha\beta} m_{\alpha} q_{\beta} \pm \omega_{\vec{q}}^0$, where $\alpha, \beta = x, y, z$, $\omega_{\vec{q}}^0$ is an even function of the wave vector \vec{q} , $D_{\alpha\beta}$ represents the DMI tensor elements, and \vec{m} is the unit vector along the net magnetization [34,35].

Due to the absence of a net magnetization in AFM materials, the Landau-Lifshitz-Gilbert (LLG) equation of motion describing their low-energy spin dynamics must be extended to include the sublattice dynamics of the antiparallel magnetic moments. Consequently, the intersublattice exchange coupling λ between the two sublattices plays an important role in the AFM resonance (AFMR) frequency, $\omega \approx \sqrt{2K\lambda}/|M_s|$ [36,37], resulting in the THz range dynamics. Here, K is the magnetocrystalline anisotropy, and $|M_s|$ is the amplitude of the magnetic moment of each sublattice. Moreover, even in the case of ferromagnets with two different magnetic elements, the sublattice dynamics result in spin nutation

^{*}Farzad.Mahfouzi@gmail.com[†]Nick.Kioussis@csun.edu

resonance [38]. Using first-principles calculations [37,39] it was also suggested that in AFM materials, the intersublattice spin exchange interaction results in a significant intersublattice Gilbert damping that is expected to play a significant role in the AFMR linewidth of the high-frequency AFMR modes.

While the DMI has been extensively studied both theoretically [40–43] and experimentally [44–49] in ferromagnetic-based bulk and interfacial systems and in multiferroic systems [50–52] where it can give rise to weak canted ferromagnetism, there have been very few investigations of the DMI in metallic antiferromagnets [53]. Motivated by the crucial role of the intersublattice dynamics in AFM materials [37,39], we have developed a computational approach of the interatomic relativistic exchange coupling [34,54] which allows us to determine both the inter- and intrasublattice contributions to the DMI in bulk \mathcal{PT} -symmetric AFM systems. Interestingly, we find that the breaking of the local mirror symmetry and the resulting local Rashba-type spin-momentum locking with opposite signs on the two sublattices yield local DMIs with opposite signs on the corresponding AFM sublattices. We investigate the effect of the sublattice DMIs on the AFM magnon dispersion and demonstrate that although the net DMI is zero, the sublattice DMIs result in nonreciprocal magnon dispersion for both low-frequency (in-plane) and high-frequency (out-of-plane) modes.

Theoretical formalism. For a system with multiple sublattices, we introduce the *general* definition of the DMI contribution to the magnetic energy in continuum theory, described by the second-order expansion with respect to the local magnetization orientation and its spatial gradient [55–59], namely,

$$E_M^{\text{GDMI}} = \sum_{ss'\alpha\beta\gamma} \int dV \mathcal{D}_{\alpha\beta,\gamma}^{ss'} m_\alpha^s \frac{\partial m_\beta^{s'}}{\partial R_\gamma}. \quad (1)$$

Here, s and s' indicate the sublattice indices, $\alpha, \beta, \gamma = x, y, z$, the expansion coefficients $\mathcal{D}_{\alpha\beta,\gamma}^{ss'}$ are the *generalized* DMI (GDMI) tensor elements, and \vec{m}_s is the unit vector along the local magnetic moment orientation of the s th sublattice. Using integration by parts in Eq. (1) yields that only the antisymmetric DMI tensor elements, $\mathcal{D}_{\alpha\beta,\gamma}^{ss'} = -\mathcal{D}_{\beta\alpha,\gamma}^{s's}$, contribute to the DMI energy, which is often referred to as the Lifshitz invariance relation. The higher-order terms in Eq. (1) in the magnetization orientation can be incorporated into an anisotropic contribution to the DMI tensor that violates the Lifshitz invariance [60].

In systems with a single sublattice, $s = s' = 1$, one can ignore the upper indices s and s' and use the Lifshitz invariance to reduce the GDMI tensor rank to the second-order conventional DMI tensor (i.e., a 3×3 matrix) through $D_{\alpha\beta} = \sum_{\gamma\gamma'} \epsilon_{\alpha\gamma\gamma'} \mathcal{D}_{\gamma\gamma',\beta} / 2$, where $\epsilon_{\alpha\gamma\gamma'}$ represents the Levi-Civita symbol [34]. However, for multisublattice systems it can be shown that only the symmetric components of the GDMI in sublattice space contribute to the conventional DMI, where $D_{\alpha\beta}^{ss'} = \sum_{\gamma\gamma'} \epsilon_{\alpha\gamma\gamma'} (\mathcal{D}_{\gamma\gamma',\beta}^{ss'} + \mathcal{D}_{\gamma\gamma',\beta}^{s's}) / 4$. As we show below, the antisymmetric intersublattice components of the GDMI in \mathcal{PT} -symmetric antiferromagnets $(\mathcal{D}_{\alpha\beta,\gamma}^{ss'} - \mathcal{D}_{\alpha\beta,\gamma}^{s's}) / 2$ can potentially be nonzero, which in turn necessitates the use of GDMI rather than the conventional DMIs.

The GDMI tensor elements are calculated using the relativistic exchange coupling, where the magnetic energy is given by

$$E_M = -\frac{1}{2} \sum_{ij:\vec{R}\vec{R}':\alpha\beta} J_{\vec{R}-\vec{R}'}^{ij,\alpha\beta} m_\alpha^i(\vec{R}) m_\beta^j(\vec{R}'). \quad (2)$$

Here, $m_\alpha^i(\vec{R})$ is the α component of the unit vector along the local magnetic moment of the i th atom in the unit cell at \vec{R} , and $J_{\vec{R}-\vec{R}'}^{ij,\alpha\beta}$ is the exchange coupling between the two local moments. The Fourier transform of the relativistic exchange coupling can be written as

$$J_{\vec{q}}^{ss',\alpha\beta} = \sum_{i \in s, j \in s': \vec{R}} J_{\vec{R}}^{ij,\alpha\beta} e^{i\vec{q} \cdot (\vec{R} + \vec{r}_i - \vec{r}_j)}, \quad (3)$$

where \vec{r}_i and \vec{r}_j are the positions of the i th and j th atoms in the unit cell and \vec{R} denotes the vector connecting two different unit cells. The GDMI tensor elements are then calculated from

$$\mathcal{D}_{\alpha\beta,\gamma}^{ss'} = \frac{1}{2V_M} \text{Im}(\partial J_{\vec{q}}^{ss',\alpha\beta} / \partial q_\gamma) |_{\vec{q}=\Gamma}, \quad (4)$$

where V_M is the unit cell volume and Γ is the center of the Brillouin zone.

Computation details. Structural relaxations were carried using the Vienna Ab initio Simulation Package (VASP) [61,62] within the generalized gradient approximation as parameterized by Perdew, Burke, and Ernzerhof (PBE) [63]. The pseudopotential and wave functions are treated within the projector augmented-wave method [64,65]. The plane wave cutoff energy is 500 eV, and a $10 \times 10 \times 10$ k -point mesh is used in the three-dimensional Brillouin zone (BZ) sampling. In order to examine the effect of the exchange correlation functional on the equilibrium structural and magnetic properties we have carried out calculations employing the local spin density approximation (LSDA) [66] as parameterized by the Perdew and Zunger [67], PBE [63], LSDA+ U and PBE+ U [68] functionals. The PBE functional was found to yield the best agreement with experiment for the structural properties of all AFM systems considered in this work and hence was used to calculate the GDMI and magnetocrystalline anisotropy (MCA).

The density functional theory calculations of the GDMI, magnetocrystalline anisotropy energy, and intersublattice exchange constant for the bulk AFM materials were carried out using the OPENMX [69–71] *ab initio* package. We adopted the Troullier-Martins-type norm-conserving pseudopotentials [72] with partial core correction and the PBE exchange correlation functional [63]. We used a $24 \times 24 \times 24$ k -point mesh in the first BZ and an energy cutoff of 350 Ry for numerical integrations in the real space grid.

Within the linear combination of the atomic orbital scheme, the multiorbital Hamiltonian $\hat{H}_{\vec{R}}$ describes the hopping of electrons between unit cells separated by distance \vec{R} . The electronic Hamiltonian for a magnetic system [34] in real space (which has the same form for both FM and AFM systems) can be written as

$$\hat{\mathbf{H}} = \hat{\mathbf{H}}^0 + \hat{\mathbf{H}}^{\text{SOC}} + \sum_{i\vec{R}} \hat{\Delta}^{i\vec{R}} \vec{m}_i(\vec{R}) \cdot \vec{\sigma}, \quad (5)$$

where the bold symbols denote matrices in real space with elements given by $[\hat{\mathbf{F}}]_{\vec{R},\vec{R}'} = \hat{F}_{\vec{R}-\vec{R}'}$ (\hat{F} denotes any operator in the Hamiltonian). Here, \hat{H}_R^0 is the paramagnetic (spin-independent) term, \hat{H}_R^{SOC} is the SOC term, and $\hat{\Delta}^{i\vec{R}}$ is the atomistic exchange splitting matrix responsible for magnetism of the i th atom. The position-dependent exchange coupling can be determined by multiplying the total exchange coupling matrix by the position operator $\hat{\Delta}^{i\vec{R}} = (\hat{1}_{i\vec{R}}\hat{\Delta} + \hat{\Delta}\hat{1}_{i\vec{R}})/2$, where $\hat{1}_{i\vec{R}}$ is the atomic position operator within the unit cell at \vec{R} [diagonal matrix elements equal to 1 for atomic orbitals of the (i, \vec{R}) th atom and zero otherwise]. Note that the SOC and exchange splitting terms are even and odd with respect to the time-reversal symmetry, respectively, which were, in turn, used to decompose the total Hamiltonian into the corresponding components.

The relativistic exchange coupling matrix elements are calculated using the Green's function method,

$$J_0^{i,zz} = \int \frac{dE}{2\pi} \text{ImTr}([\hat{\Delta}\hat{G} + \hat{G}\hat{\Delta}]_{\vec{R}=0} \hat{\sigma}^z \hat{1}_i) f(E), \quad (6a)$$

$$J_{\vec{R}}^{ij,\alpha\beta} = \frac{1}{4\pi} \int dE \text{ImTr}([\hat{\Delta}\hat{G}]_{\vec{R}} \hat{1}_i \hat{\sigma}^\alpha [\hat{\Delta}\hat{G}]_{-\vec{R}} \hat{\sigma}^\beta \hat{1}_j + [\hat{G}\hat{\Delta}]_{\vec{R}} \hat{1}_i \hat{\sigma}^\alpha [\hat{G}\hat{\Delta}]_{-\vec{R}} \hat{\sigma}^\beta \hat{1}_j + [\hat{\Delta}\hat{G}\hat{\Delta}]_{\vec{R}} \hat{1}_i \hat{\sigma}^\alpha [\hat{G}]_{-\vec{R}} \hat{\sigma}^\beta \hat{1}_j + [\hat{G}]_{\vec{R}} \hat{1}_i \hat{\sigma}^\alpha [\hat{\Delta}\hat{G}\hat{\Delta}]_{-\vec{R}} \hat{\sigma}^\beta \hat{1}_j) f(E). \quad (6b)$$

Here, $[\hat{F}\hat{G}]_{\vec{R}} = \frac{1}{N_k} \sum_{\vec{k}} \hat{F}_{\vec{k}} \hat{G}_{\vec{k}} e^{-i\vec{k}\cdot\vec{R}}$ (\hat{F} and \hat{G} denote any two operators in the integrand), N_k is the number of k points, $f(E)$ is the Fermi-Dirac distribution function, and

$$\hat{G}_{\vec{k}} = (E\hat{O}_{\vec{k}} - \hat{H}_{\vec{k}})^{-1} \quad (7)$$

is the Green's function, where the Fourier transformed Hamiltonian $\hat{H}_{\vec{k}} = \sum_{\vec{R}} \hat{H}_{\vec{R}} e^{i\vec{k}\cdot\vec{R}}$ and, similarly, the overlap $\hat{O}_{\vec{k}}$ matrices are calculated using the linear combination of pseudoatomic orbital approach as implemented in the OPENMX package [69–71]. The pseudoatomic orbitals are Mn6.0-s3p2d1, Au7.0-s3p2d1, Cu6.0S-s3p2d1, As7.0-s3p2d1, and Pd7.0-s3p2d1 (see [73] for details), where in the abbreviation of the basis functions, such as X5.0-s1p1, X denotes the atomic element, 5.0 denotes the cutoff radius in the generation by the confinement scheme, and s1p1 means that the calculations are carried out using one orbital for each of the s and p atomic orbitals. In the calculation of the exchange coupling the energy integration in Eq. (6a) was carried out using the Matsubara summation approach with the poles obtained from Ozaki's continued fraction method of the Fermi-Dirac distribution function [74]. The Fermi-Dirac distribution function temperature was set at $k_B T = 25$ meV, and 60 poles were employed for the Matsubara summation.

The uniaxial MCA constants K_u^x and K_u^y are calculated using the torque approach for single domain magnetization [75].

Results and discussion. We find that the total GDMI $\mathcal{D}_{\alpha\beta,\gamma}^{\text{tot}} = \sum_{ss'} \mathcal{D}_{\alpha\beta,\gamma}^{ss'}$ vanishes for \mathcal{PT} -symmetric materials where the global mirror symmetry is preserved. Consequently, the intra- and intersublattice tensor elements satisfy $\mathcal{D}_{\alpha\beta,\gamma}^{\uparrow\uparrow} = -\mathcal{D}_{\alpha\beta,\gamma}^{\downarrow\downarrow}$ and $\mathcal{D}_{\alpha\beta,\gamma}^{\uparrow\downarrow} = -\mathcal{D}_{\alpha\beta,\gamma}^{\downarrow\uparrow}$. The numerical results of the relativistic exchange coupling reveal that the nonzero

relativistic GDMI tensor elements are of the form

$$\mathcal{D}_{\alpha\beta,\gamma}^{ss'} = -\mathcal{D}_{\beta\alpha,\gamma}^{s's} = \delta_{\alpha\gamma} \vec{D}_g^{ss'} \cdot (\vec{e}_\beta \times \vec{e}_\alpha). \quad (8)$$

Here, $\vec{D}_g^{ss'}$ are the sublattice matrix elements of the GDMI vector, $\delta_{\alpha\gamma}$ is the Kronecker delta, and $\vec{e}_{\alpha(\beta)}$ is the unit vector along the α (β) direction. Throughout the remainder of this Letter we denote the antisymmetric intersublattice GDMI as $\vec{D}_{g,as}^{\uparrow\downarrow}$. We also find that the Lifshitz invariance identity $\mathcal{D}_{\alpha\beta,\alpha}^{ss'} = -\mathcal{D}_{\beta\alpha,\alpha}^{s's}$ is satisfied in the numerical calculations. Note that, in the case of Néel-type DMIs the unit vector \vec{e}_β points along the broken local mirror symmetry direction. Therefore, for an AFM with broken local mirror symmetry along, e.g., the z axis, the GDMI vector $\vec{D}_g^{ss'}$ lies in the xy plane.

In addition to the fact that $\vec{D}_{g,as}^{\uparrow\downarrow}$ does not contribute to the conventional DMI $\mathcal{D}_{\alpha\beta}^{ss'}$, it can also be shown that the antisymmetric intersublattice GDMI elements do not originate from the antisymmetric interatomic exchange coupling (i.e., interatomic DMI), where the magnetic energy can be written as $E_{\text{DMI}} = \sum_{ij} \vec{d}_{ij} \cdot \vec{m}_i \times \vec{m}_j$ (i, j denote atomic sites). In this case, the corresponding contribution to the relativistic exchange coupling for a system with broken mirror symmetry along the z axis is given by $J_{\text{DMI}}^{ij,\alpha\beta} = \sum_{\gamma} \epsilon_{\alpha\beta\gamma} d_{ij}^{\gamma}$, where $\vec{d}_{ij} = d_{r_{ij}}^N \vec{e}_z \times \vec{r}_{ij}/r_{ij}$ and $d_{r_{ij}}^N$ is the atomistic Néel DMI strength between two atoms separated by \vec{r}_{ij} . The presence of the Levi-Civita symbol in the relativistic exchange coupling results in GDMI tensor elements that obey $\mathcal{D}_{\alpha\beta,\gamma}^{ss'} = -\mathcal{D}_{\beta\alpha,\gamma}^{s's}$, leading to a *symmetric* contribution to the intersublattice GDMI vector, $\vec{D}_g^{\uparrow\downarrow} = \vec{D}_g^{\downarrow\uparrow}$, which is absent in Eq. (8). This suggests that the antisymmetric GDMI term in Eq. (8) originates from the off-diagonal components of the anisotropic interatomic exchange coupling and therefore should not be confused with the conventional intersublattice DMI present in systems with broken global mirror symmetry. The unconventional nature of the intersublattice GDMI is further demonstrated below, where we find that it varies quadratically with the SOC, in sharp contrast to the linear SOC dependence of the conventional DMI [28].

In addition to the nonzero matrix elements in Eq. (8), we find finite values for $\mathcal{D}_{\alpha\alpha,\beta}^{ss}$, which are of nonrelativistic origin and arise from the variation of the intersublattice exchange coupling between successive Mn layers along the locally broken mirror symmetry direction. This can be understood using a one-dimensional magnetic chain along the z axis with two magnetic moments within the unit cell at the origin and the relative position b/a , where a is the length of the unit cell. Considering staggered intra- and intercell exchange interactions, J_1 and J_2 , respectively, and using Eqs. (3) and (4), we find $J_{q_z}^{12,zz} = (J_{q_z}^{21,zz})^* = e^{-iq_z b} (J_1 + J_2 e^{iq_z a})$ and $D_{zz,z}^{12} \propto (a-b)J_1 - bJ_2$. It should be noted that the last term appears in the off-diagonal elements of the magnon Hamiltonian and does not yield a nonreciprocal dispersion to the magnon band structure.

Table I lists the calculated values of the relaxed lattice constants, magnetic moment, uniaxial MCA, and sublattice GDMI tensor elements $\vec{D}_g^{\uparrow\uparrow}$ and $\vec{D}_{g,as}^{\uparrow\downarrow}$ for Mn₂Au (space group $I4/mmm$), MnPd₂ (space group $Pnma$), tetragonal MnCuAs (space group $P4/nmm$), and orthorhombic MnCuAs

TABLE I. Equilibrium lattice constants a , b , and c , magnetic moment of the Mn atom $|M_{\text{Mn}}|$, uniaxial magnetocrystalline anisotropy energies K_u^x and K_u^y per formula unit, and intrasublattice ($\vec{D}_g^{\uparrow\uparrow} = -\vec{D}_g^{\downarrow\downarrow}$) and antisymmetric intersublattice ($\vec{D}_{g,as}^{\uparrow\downarrow}$) GDMI vectors for Mn_2Au , MnPd_2 , tetragonal MnCuAs , and orthorhombic MnCuAs . The numbers in parentheses denote the experimentally reported values.

	a (Å)	b (Å)	c (Å)	$ M_{\text{Mn}} $ (in units of μ_B)	$K_u^{x,y}$ ($\frac{\text{meV}}{\text{f.u.}}$)	$\vec{D}_g^{\uparrow\uparrow}$ (mJ/m ²)	$\vec{D}_{g,as}^{\uparrow\downarrow}$ ($\mu\text{J}/\text{m}^2$)
Mn_2Au	3.28 (3.32) ^a	3.28 (3.32) ^a	8.43 (8.53) ^a	3.5	-2.5, -2.5	(0.11, 0.11, 0)	(130, 130, 0)
MnPd_2	3.99 (4.03) ^b	5.49 (5.46) ^b	8.28 (8.13) ^b	3.88	-0.08, 0.05	(-0.11, 0, 0.2)	(17, 0, -20)
Tetragonal MnCuAs	3.68 (3.8) ^c	3.68 (3.8) ^c	6.4 (6.3) ^c	3.4	-0.17, -0.17	(-1.13, -1.13, 0)	(-10, -10, 0)
Orthorhombic MnCuAs	3.8 (3.86) ^d	6.45 (6.58) ^d	7.29 (7.3) ^d	3.6	-0.08, -0.11	(-0.41, -0.44, 0)	(8, 3, 0)

^aReference [76]; ^bRef. [77]; ^cRef. [78]; ^dRef. [79].

(space group $Pnma$). The corresponding broken local mirror symmetry planes of the crystal structures are shown in Figs. 1(a)–1(d), respectively. The numbers in parentheses denote the corresponding experimentally reported values. Overall, there is good agreement for the lattice constants and the magnetic moments. The negative MCAs suggest in-plane magnetic anisotropy for all four compounds, which are also in agreement with the experimental observations. Interestingly, for Mn_2Au , $\vec{D}_g^{\uparrow\uparrow} \approx \vec{D}_{g,as}^{\uparrow\downarrow}$, while for the remaining antiferromagnets the intersublattice GDMI is much smaller than the intrasublattice DMI.

The GDMI vectors for Mn_2Au and tetragonal MnCuAs are isotropic in the xy plane due to their tetragonal crystal structure, while for orthorhombic MnCuAs the intrasublattice GDMI is slightly anisotropic. On the other hand, for MnPd_2 the GDMI vector lies on the xz plane because the local mirror symmetry is broken along the y axis, with the x and z components having opposite signs.

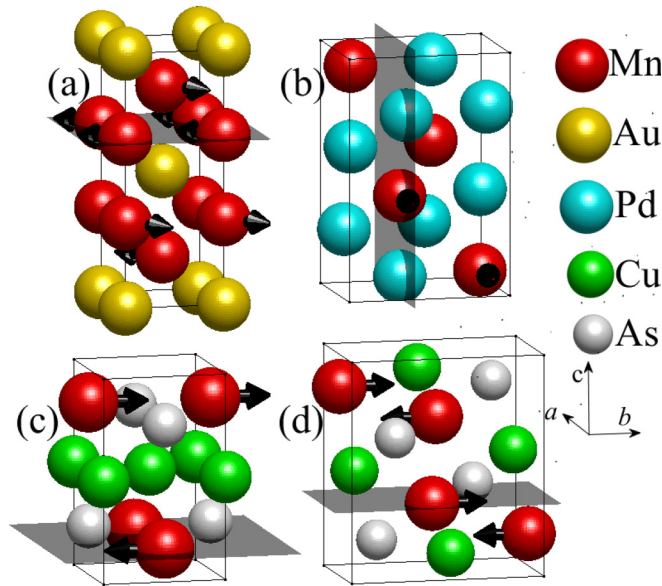


FIG. 1. Crystal structures of collinear PT -symmetric antiferromagnets: (a) Mn_2Au (space group $I4/mmm$), (b) MnPd_2 (space group $Pnma$), (c) tetragonal MnCuAs (space group $P4/nmm$), and (d) orthorhombic MnCuAs (space group $Pnma$). The arrows denote the direction of the magnetic moments, and the gray planes denote the sublattice planes which break the local mirror symmetry.

In order to understand the underlying mechanism for the sublattice-resolved GDMI in Mn_2Au , where $\vec{D}_g^{\uparrow\uparrow} \approx \vec{D}_{g,as}^{\uparrow\downarrow}$, we show in Figs. 2(a) and 2(b) the x component of the intrasublattice GDMI on the Mn_\uparrow sublattice and the intersublattice GDMI, respectively, as a function of chemical potential shift. Turning on the SOC only for the Mn_\downarrow (Au) layers results in a negative (positive) contribution to $\vec{D}_g^{\uparrow\uparrow} \cdot \hat{e}_x$ on the Mn_\uparrow sublattice, while the SOC of the Mn_\uparrow layer yields a relatively negligible contribution. The opposite signs of the Mn_\downarrow (dashed black curve) and Au (red curve) layer contributions reduce in turn the total $\vec{D}_g^{\uparrow\uparrow} \cdot \hat{e}_x$. We find that the contribution of the Mn_\downarrow layer is relatively insensitive to chemical potential, while that of the Au layer increases with decreasing chemical potential due to the depletion of electrons from the fully occupied Au d orbitals, resulting in sign reversal of the total $\vec{D}_g^{\uparrow\uparrow} \cdot \hat{e}_x$ with hole doping. On the other hand, the variation of $\vec{D}_{g,as}^{\uparrow\downarrow} \cdot \hat{e}_x$ with the chemical potential in Fig. 2(b) shows the intersublattice GDMI originates primarily from the Au atoms since the contributions from the two Mn sublattices cancel out. Note that the relatively small difference between the total

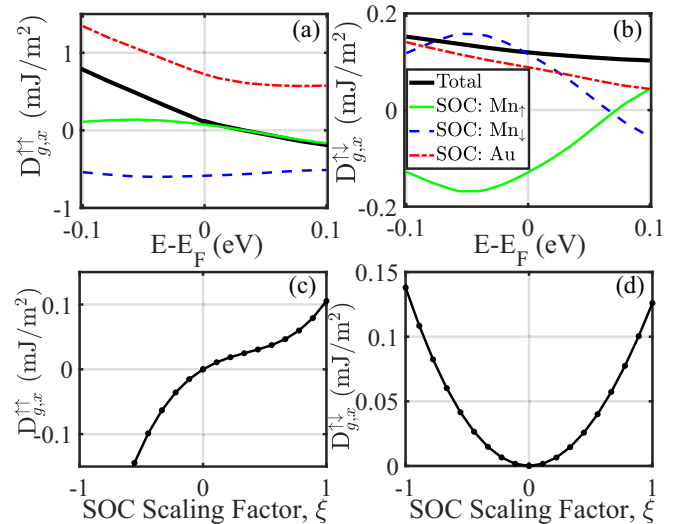


FIG. 2. (a) Intrasublattice and (b) intersublattice bulk GDMI in Mn_2Au versus shift of the chemical potential. The intrasublattice GDMI corresponds to the spin-up Mn atoms. The green, blue, and red curves denote the layer-resolved DMIs when only the SOC of the spin-up Mn, spin-down Mn, and Au atoms are turned on, respectively. (c) Intrasublattice and (d) intersublattice GDMI in Mn_2Au versus the SOC scaling factor.

GDMI and the sum of the atom-resolved contributions is due to the fact that the atomic decomposition is accurate only to first-order perturbation in SOC.

In Figs. 2(c) and 2(d) we present the results for the intra- and intersublattice GDMI versus the SOC scaling factor which multiplies the second term of the Hamiltonian in Eq. (5). We find that, as expected from an observable that originates from the broken local mirror symmetry and local Rashba-type spin-momentum locking, the intrasublattice GDMI is to the lowest order a linear function of SOC. In sharp contrast, the intersublattice GDMI exhibits an even dependence on the SOC which is uncharacteristic of the DMI and resembles the quadratic SOC dependence of the anisotropic exchange coupling. The absence of a conventional contribution to the intersublattice GDMI can be understood by the fact that the two sublattices are connected through a local mirror symmetry operation.

Magnon dispersion. In the absence of an external magnetic field, the atomistic spin dynamics are governed by the LLG equation of motion for magnetization dynamics around the equilibrium configuration, $\vec{m}_0^s(\vec{R}) = m_z^s \vec{e}_z$,

$$\frac{M_s}{2} \frac{\partial \vec{m}^s(\vec{R})}{\partial t} = -\vec{m}^s(\vec{R}) \times \vec{B}_{\text{eff}}^{\vec{R},s}, \quad (9)$$

where $m_z^s = \pm 1$ and the effective magnetic field experienced by the sublattice s at position \vec{R} is given by

$$\vec{B}_{\text{eff}}^{\vec{R},s} = J_0^{s,zz} \vec{e}_z + \sum_{s'\vec{R}'} J_{\vec{R}-\vec{R}'}^{ss',\alpha\beta} m_{\alpha}^{s'}(\vec{R}') \vec{e}_{\beta}, \quad (10)$$

with $\alpha, \beta = x, y$. The magnon dispersion can be obtained by solving the linearized LLG equation around the equilibrium magnetization direction m_z^s and Fourier transforming both in time and space,

$$\frac{M_s}{2} i\omega m_{x,\vec{q}}^s = m_z^s \sum_{s'\alpha} J_{\vec{q}}^{ss',\alpha y} m_{\alpha,\vec{q}}^{s'} - m_{y,\vec{q}}^s J_0^{s,zz}, \quad (11a)$$

$$\frac{M_s}{2} i\omega m_{y,\vec{q}}^s = m_{x,\vec{q}}^s J_0^{s,zz} - m_z^s \sum_{s'\alpha} J_{\vec{q}}^{ss',\alpha x} m_{\alpha,\vec{q}}^{s'}. \quad (11b)$$

It should be noted that in order to observe effects of a Néel-type DMI on the magnon dispersion, the direction of the equilibrium magnetic moments should be perpendicular to the direction of broken local mirror symmetry. A generalization of the above to an arbitrary orientation for the equilibrium magnetization direction is straightforward. The magnon band structure $\omega_{\vec{q}}$ along the high-symmetry directions for Mn₂Au with Néel ordering pointed along the x axis is displayed in Fig. 3(a), with the corresponding nonreciprocal component $\omega_{\vec{q}}^{nr} = (\omega_{\vec{q}} - \omega_{-\vec{q}})/2$ shown in Fig. 3(b). The dashed blue (solid red) dispersion curves correspond to the out-of-plane (in-plane) mode. Similar to the ferromagnetic case, the slope of the nonreciprocal magnon dispersion at the Γ point yields the DMI. A nonzero value for the nonreciprocal magnon dispersion can be seen for magnons propagating along the Y direction, which is perpendicular to both the Néel ordering orientation and the broken local mirror symmetry axis (i.e., z axis).

The different slopes of the two modes at Γ can be understood using the analytical expression for the magnon

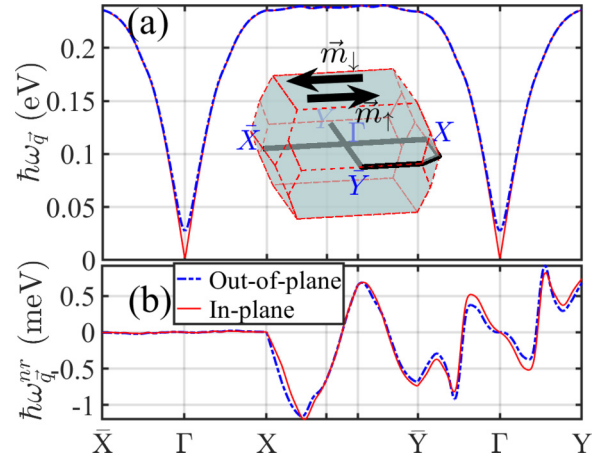


FIG. 3. (a) Magnon dispersion for Mn₂Au along high-symmetry directions with the Néel ordering vector along x ; (b) corresponding nonreciprocal component, $\omega_{\vec{q}}^{nr} = (\omega_{\vec{q}} - \omega_{-\vec{q}})/2$, versus high-symmetry directions. The solid blue (dash-dotted red) curves correspond to the in-plane (out-of-plane) mode. Inset: Brillouin zone and the corresponding high-symmetry directions.

dispersion which can be obtained by the eigenfrequencies of the 4×4 matrix given by Eqs. (11a) and (11b), which are of the form

$$\frac{1}{2}|M_s|\omega_{\vec{q}}^{\pm} = \text{Im}(J_{\vec{q}}^{\uparrow\uparrow,xy}) \pm \text{Im}(J_{\vec{q},as}^{\downarrow\downarrow,xy}) + \omega_{\vec{q}}^{0,\pm}, \quad (12)$$

where, in the derivation we used, $J_{\vec{q},as}^{\downarrow\downarrow,xy} = -J_{\vec{q},as}^{\uparrow\uparrow,xy}$, $J_{\vec{q}}^{\downarrow\downarrow,xy} = -J_{\vec{q}}^{\uparrow\uparrow,xy}$, and

$$(\omega_{\vec{q}}^{0,\pm})^2 = (J_{\vec{q}}^{\uparrow\uparrow,xx} - J_0^{\uparrow,zz} \mp J_{\vec{q}}^{\uparrow\downarrow,xx}) \times (J_{\vec{q}}^{\uparrow\uparrow,yy} - J_0^{\uparrow,zz} \pm J_{\vec{q}}^{\uparrow\downarrow,yy}) \quad (13)$$

is an even function of \vec{q} and at $\vec{q} = \Gamma$ yields Kittel's AFMR expression [36,37]. The identical contribution of the intrasublattice GDMI, $\text{Im}(J_{\vec{q}}^{\uparrow\uparrow,xy})$, to both magnon modes can be readily seen in the limit of independent sublattice dynamics, whereby the two sublattices and the two corresponding magnon modes are assumed to be completely independent, with the nonreciprocal components given by $\omega_{\vec{q}}^{s,nr} = \sum_{\alpha\beta} D_{\alpha\beta}^{ss} m_{\alpha}^s q_{\beta}$ [34]. Since the magnetic moments of the two sublattices are antiparallel, $m_{\alpha}^{\uparrow} = -m_{\alpha}^{\downarrow}$, and the intrasublattice GDMI tensor elements have opposite signs, $D_{\alpha\beta}^{\uparrow\uparrow} = -D_{\alpha\beta}^{\downarrow\downarrow}$, we obtain $\omega_{\vec{q}}^{\uparrow,nr} = \omega_{\vec{q}}^{\downarrow,nr}$. This is in contrast to the effect of the total DMI $(D_{\alpha\beta}^{\uparrow\uparrow} + D_{\alpha\beta}^{\downarrow\downarrow})/2$, which is nonzero in systems with broken global mirror symmetry and results in the shift of the two magnons in opposite directions and their hybridization at the Γ point [80]. It is also worth noting that in the absence of MCA where the dispersion is given by $\omega_{\vec{q}}^0 \propto |\vec{q}|$, the nonreciprocal component of the magnon dispersion, e.g., $\omega_{\vec{q}}^{nr} \propto q_x$, resulting from the alternating intrasublattice DMI $D^{\uparrow\uparrow} = -D^{\downarrow\downarrow}$ does not shift the position of the minima of the magnon dispersion at the Γ point but instead yields an asymmetric change in the slopes of the magnon dispersion propagating along opposite directions, resulting in an antisymmetric V-shaped dispersion.

In summary, a first principles study based on the Green's function approach was presented for the DMI of a family of AFM materials with broken local mirror symmetry, including Mn_2Au , MnCuAs , and MnPd_2 , which allowed the separation of the intra- and intersublattice contributions to the generalized DMI. For the prototype Mn_2Au we elucidated the atomistic origin of the sublattice GDMI by turning on the SOC on specific atoms. We demonstrated that the intrasublattice GDMI of the Mn_\uparrow sublattice arises from the interplay of the Au and spin-down Mn_\downarrow atom-resolved contributions, which have opposite signs for a wide range of the chemical potential shift. On the other hand, the source of the intersublattice GDMI is due solely to the Au atoms. Furthermore, we showed that the intrasublattice GDMI, which is the dominant component, has a linear dependence on SOC and contributes

equally to both in-plane and out-of-plane magnon modes. In contrast, the intersublattice GDMI tensor elements depend quadratically on the SOC, and although they share the same microscopic origin as the anisotropic exchange coupling, they make a nonreciprocal contribution to the magnon dispersion. Our theoretical predictions of the difference in nonreciprocal magnon dispersion for the two modes can be used to measure the sublattice components of the GDMI tensor elements.

Acknowledgments. The authors are grateful for fruitful discussions with O. V. Gomonay and J. Sinova. The work is supported by NSF ERC-Translational Applications of Nanoscale Multiferroic Systems (TANMS) Grant No. 1160504 and by NSF Partnership in Research and Education in Materials (PREM) Grant No. DMR-1205734.

- [1] V. Baltz, A. Manchon, M. Tsoi, T. Moriyama, T. Ono, and Y. Tserkovnyak, Antiferromagnetic spintronics, *Rev. Mod. Phys.* **90**, 015005 (2018).
- [2] E. V. Gomonay and V. M. Loktev, Spintronics of antiferromagnetic systems (review article), *Low Temp. Phys.* **40**, 17 (2014).
- [3] T. Jungwirth, J. Sinova, A. Manchon, X. Marti, J. Wunderlich, and C. Felser, The multiple directions of antiferromagnetic spintronics, *Nat. Phys.* **14**, 200 (2018).
- [4] J. Železný, P. Wadley, K. Olejník, A. Hoffmann, and H. Ohno, Spin transport and spin torque in antiferromagnetic devices, *Nat. Phys.* **14**, 220 (2018).
- [5] L. Šmejkal, Y. Mokrousov, B. Yan, and A. H. MacDonald, Topological antiferromagnetic spintronics, *Nat. Phys.* **14**, 242 (2018).
- [6] J. Železný, H. Gao, K. Výborný, J. Zemen, J. Mašek, A. Manchon, J. Wunderlich, J. Sinova, and T. Jungwirth, Relativistic Néel-Order Fields Induced by Electrical Current in Antiferromagnets, *Phys. Rev. Lett.* **113**, 157201 (2014).
- [7] S. Y. Bodnar, L. Šmejkal, I. Turek, T. Jungwirth, O. Gomonay, J. Sinova, A. A. Sapozhnik, H.-J. Elmers, M. Kläui, and M. Jourdan, Writing and reading antiferromagnetic Mn_2Au by Néel spin-orbit torques and large anisotropic magnetoresistance, *Nat. Commun.* **9**, 348 (2018).
- [8] A. Manchon, J. Železný, I. M. Miron, T. Jungwirth, J. Sinova, A. Thiaville, K. Garello, and P. Gambardella, Current-induced spin-orbit torques in ferromagnetic and antiferromagnetic systems, *Rev. Mod. Phys.* **91**, 035004 (2019).
- [9] P. Wadley *et al.*, Electrical switching of an antiferromagnet, *Science* **351**, 587 (2016).
- [10] M. J. Grzybowski, P. Wadley, K. W. Edmonds, R. Beardsley, V. Hills, R. P. Champion, B. L. Gallagher, J. S. Chauhan, V. Novak, T. Jungwirth, F. Maccheronzi, and S. S. Dhesi, Imaging Current-Induced Switching of Antiferromagnetic Domains in CuMnAs , *Phys. Rev. Lett.* **118**, 057701 (2017).
- [11] V. Saidl, P. Nemeč, P. Wadley, V. Hills, R. P. Champion, V. Novak, K. W. Edmonds, F. Maccheronzi, S. S. Dhesi, B. L. Gallagher, F. Trojanek, J. Kunes, J. Železný, P. Maly, and T. Jungwirth, Optical determination of the Néel vector in a CuMnAs thin-film antiferromagnet, *Nat. Photonics* **11**, 91 (2017).
- [12] Z. Sun, Y. Yi, T. Song, G. Clark, B. Huang, Y. Shan, S. Wu, D. Huang, C. Gao, Z. Chen, M. McGuire, T. Cao, D. Xiao, W.-T. Liu, W. Yao, X. Xu, and S. Wu, Giant nonreciprocal second harmonic generation from layered antiferromagnetic bilayer CrI_3 , *Nature (London)* **572**, 497 (2019).
- [13] H. Chen, Q. Niu, and A. H. MacDonald, Anomalous Hall Effect Arising from Noncollinear Antiferromagnetism, *Phys. Rev. Lett.* **112**, 017205 (2014).
- [14] S. Nakatsuji, N. Kiyohara, and T. Higo, Large anomalous Hall effect in a non-collinear antiferromagnet at room temperature, *Nature (London)* **527**, 212 (2015).
- [15] A. K. Nayak, J. E. Fischer, Y. Sun, B. Yan, J. Karel, A. C. Komarek, C. Shekhar, N. Kumar, W. Schnelle, J. Kübler, C. Felser, and S. P. P. Parkin, Large anomalous Hall effect driven by a nonvanishing Berry curvature in the noncollinear antiferromagnet Mn_3Ge , *Sci. Adv.* **2**, e1501870 (2016).
- [16] J. Sklenar, W. Zhang, M. B. Jungfleisch, W. Jiang, H. Saglam, J. E. Pearson, J. B. Ketterson, and A. Hoffmann, Spin hall effects in metallic antiferromagnets-perspectives for future spin orbitronics, *AIP Adv.* **6**, 055603 (2016).
- [17] W. Zhang, M. B. Jungfleisch, W. Jiang, J. E. Pearson, A. Hoffmann, F. Freimuth, and Y. Mokrousov, Spin Hall Effects in Metallic Antiferromagnets, *Phys. Rev. Lett.* **113**, 196602 (2014).
- [18] D.-F. Shao, G. Gurung, S.-H. Zhang, and E. Y. Tsymbal, Dirac Nodal Line Metal for Topological Antiferromagnetic Spintronics, *Phys. Rev. Lett.* **122**, 077203 (2019).
- [19] A. M. Jones, H. Yu, J. S. Ross, P. Klement, N. J. Ghimire, J. Yan, D. G. Mandrus, W. Yao, and X. Xu, Spin-layer locking effects in optical orientation of exciton spin in bilayer WSe_2 , *Nat. Phys.* **10**, 130 (2014).
- [20] M. Gehlmann, I. Aguilera, G. Bihlmayer, E. Młyńczak, M. Eschbach, S. Döring, P. Gospodaric, S. Cramm, B. Kardynał, L. Plucinski, S. Blügel, and C. M. Schneider, Quasi 2D electronic states with high spin-polarization in centrosymmetric MoS_2 bulk crystals, *Sci. Rep.* **6**, 26197 (2016).
- [21] T. Das and A. V. Balatsky, Engineering three-dimensional topological insulators in Rashba-type spin-orbit coupled heterostructures, *Nat. Commun.* **4**, 1972 (2013).
- [22] W. A. Atkinson, Microscopic model for the hidden Rashba effect in $\text{YBa}_2\text{Cu}_3\text{O}_{6+x}$, *Phys. Rev. B* **101**, 024513 (2020).
- [23] L. Yuan, Q. Liu, X. Zhang, J.-W. Luo, S.-S. Li, and A. Zunger, Uncovering and tailoring hidden Rashba spin-orbit splitting in centrosymmetric crystals, *Nat. Commun.* **10**, 906 (2019).
- [24] S. Lee and Y.-K. Kwon, Unveiling giant hidden Rashba effects in two-dimensional Si_2Bi_2 , *npj 2D Mater. Appl.* **4**, 45 (2020).

- [25] S. Selzer, L. Salemi, A. Deák, E. Simon, L. Szunyogh, P. M. Oppeneer, and U. Nowak, Current-induced switching of antiferromagnetic order in Mn_2Au from first principles, *Phys. Rev. B* **105**, 174416 (2022).
- [26] C. Ederer and N. A. Spaldin, Towards a microscopic theory of toroidal moments in bulk periodic crystals, *Phys. Rev. B* **76**, 214404 (2007).
- [27] F. Thöle, A. Keliri, and N. A. Spaldin, Concepts from the linear magnetoelectric effect that might be useful for antiferromagnetic spintronics, *J. Appl. Phys.* **127**, 213905 (2020).
- [28] I. J. Dzyaloshinsky, A thermodynamic theory of “weak” ferromagnetism of antiferromagnetics, *J. Phys. Chem. Solids* **4**, 241 (1958).
- [29] T. Moriya, Anisotropic superexchange interaction and weak ferromagnetism, *Phys. Rev.* **120**, 91 (1960).
- [30] A. Fert, V. Cros, and J. Sampaio, Skyrmions on the track, *Nat. Nanotechnol.* **8**, 152 (2013).
- [31] N. S. Kiselev, A. N. Bogdanov, R. Schäfer, and U. K. Röbber, Chiral skyrmions in thin magnetic films: New objects for magnetic storage technologies? *J. Phys. D* **44**, 392001 (2011).
- [32] N. Nagaosa and Y. Tokura, Topological properties and dynamics of magnetic skyrmions, *Nat. Nanotechnol.* **8**, 899 (2013).
- [33] G. Gitgeatpong, Y. Zhao, P. Piyawongwatthana, Y. Qiu, L. W. Harriger, N. P. Butch, T. J. Sato, and K. Matan, Nonreciprocal Magnons and Symmetry-Breaking in the Noncentrosymmetric Antiferromagnet, *Phys. Rev. Lett.* **119**, 047201 (2017).
- [34] F. Mahfouzi and N. Kioussis, First-principles calculation of the Dzyaloshinskii-Moriya interaction: A Green’s function approach, *Phys. Rev. B* **103**, 094410 (2021).
- [35] T. Koretsune, T. Kikuchi, and R. Arita, First-Principles Evaluation of the Dzyaloshinskii-Moriya Interaction, *J. Phys. Soc. Jpn.* **87**, 041011 (2018).
- [36] F. Keffer and C. Kittel, Theory of Antiferromagnetic Resonance, *Phys. Rev.* **85**, 329 (1952).
- [37] F. Mahfouzi and N. Kioussis, Damping and antidamping phenomena in metallic antiferromagnets: An *ab initio* study, *Phys. Rev. B* **98**, 220410(R) (2018).
- [38] K. Neeraj, N. Awari, S. Kovalev, D. Polley *et al.*, Inertial spin dynamics in ferromagnets, *Nat. Phys.* **17**, 245 (2021).
- [39] Q. Liu, H. Y. Yuan, K. Xia, and Z. Yuan, Mode-dependent damping in metallic antiferromagnets due to intersublattice spin pumping, *Phys. Rev. Mater.* **1**, 061401(R) (2017).
- [40] H. Yang, A. Thiaville, S. Rohart, A. Fert, and M. Chshiev, Anatomy of Dzyaloshinskii-Moriya Interaction at Co/Pt Interfaces, *Phys. Rev. Lett.* **115**, 267210 (2015).
- [41] B. Zimmermann, G. Bihlmayer, M. Böttcher, M. Bouhassoune, S. Lounis, J. Sinova, S. Heinze, S. Blügel, and B. Dupe, Comparison of first-principles methods to extract magnetic parameters in ultrathin films: Co/Pt(111), *Phys. Rev. B* **99**, 214426 (2019).
- [42] S. Mankovsky and H. Ebert, Accurate scheme to calculate the interatomic Dzyaloshinskii-Moriya interaction parameters, *Phys. Rev. B* **96**, 104416 (2017).
- [43] F. Freimuth, S. Blügel, and Y. Mokrousov, Relation of the Dzyaloshinskii-Moriya interaction to spin currents and to the spin-orbit field, *Phys. Rev. B* **96**, 054403 (2017).
- [44] S. Mühlbauer, B. Binz, F. Jonietz, C. Pfleiderer, A. Rosch, A. Neubauer, R. Georgii, and P. Böni, Skyrmion lattice in a chiral magnet, *Science* **323**, 915 (2009).
- [45] A. Cao, X. Zhang, B. Koopmans, S. Peng, Y. Zhang, Z. Wang, S. Yan, H. Yang, and W. Zhao, Tuning the Dzyaloshinskii/Moriya interaction in Pt/Co/MgO heterostructures through the MgO thickness, *Nanoscale* **10**, 12062 (2018).
- [46] J. Cho, N.-H. Kim, S. Lee, J.-S. Kim, R. Lavrijsen, A. Solignac, Y. Yin, D.-S. Han, N. J. J. van Hoof, H. J. M. Swagten, B. Koopmans, and C.-Y. You, Thickness dependence of the interfacial Dzyaloshinskii-Moriya interaction in inversion symmetry broken systems, *Nat. Commun.* **6**, 7635 (2015).
- [47] X. Ma, G. Yu, C. Tang, X. Li, C. He, J. Shi, K. L. Wang, and X. Li, Interfacial Dzyaloshinskii-Moriya Interaction: Effect of $5d$ Band Filling and Correlation with Spin Mixing Conductance, *Phys. Rev. Lett.* **120**, 157204 (2018).
- [48] M. Belmeguenai, J.-P. Adam, Y. Roussigné, S. Eimer, T. Devolder, J.-V. Kim, S. M. Cherif, A. Stashkevich, and A. Thiaville, Interfacial Dzyaloshinskii-Moriya interaction in perpendicularly magnetized Pt/Co/ AlO_x ultrathin films measured by Brillouin light spectroscopy, *Phys. Rev. B* **91**, 180405(R) (2015).
- [49] N.-H. Kim, J. Cho, J. Jung, D.-S. Han, Y. Yin, J.-S. Kim, H. J. M. Swagten, K. Lee, M.-H. Jung, and C.-Y. You, Role of top and bottom interfaces of a Pt/Co/ AlO_x system in Dzyaloshinskii-Moriya interaction, interface perpendicular magnetic anisotropy, and magneto-optical Kerr effect, *AIP Adv.* **7**, 035213 (2017).
- [50] N. A. Spaldin and R. Ramesh, Advances in magnetoelectric multiferroics, *Nat. Mater.* **18**, 203 (2019).
- [51] M. Fiebig, T. Lottermoser, D. Meier, and M. Trassin, The evolution of multiferroics, *Nat. Rev. Mater.* **1**, 16046 (2016).
- [52] D. Treves, Magnetic studies of some orthoferrites, *Phys. Rev.* **125**, 1843 (1962).
- [53] Md. R. K. Akanda, I. J. Park, and R. K. Lake, Interfacial Dzyaloshinskii-Moriya interaction of antiferromagnetic materials, *Phys. Rev. B* **102**, 224414 (2020).
- [54] H. Ebert and S. Mankovsky, Anisotropic exchange coupling in diluted magnetic semiconductors: *Ab initio* spin-density functional theory, *Phys. Rev. B* **79**, 045209 (2009).
- [55] A. N. Bogdanov and U. K. Röbber, Chiral Symmetry Breaking in Magnetic Thin Films and Multilayers, *Phys. Rev. Lett.* **87**, 037203 (2001).
- [56] L. D. Landau and L. P. Pitaevskii, *Electrodynamics of Continuous Media* (Pergamon, Oxford, 1984).
- [57] A. N. Bogdanov and D. A. Yablonskii, Contribution to the theory of inhomogeneous states of magnets in the region of magnetic-field-induced phase transitions. Mixed state of antiferromagnets, *Zh. Eksp. Teor. Fiz.* **96**, 253 (1989).
- [58] K. M. D. Hals and K. Everschor-Sitte, New Boundary-Driven Twist States in Systems with Broken Spatial Inversion Symmetry, *Phys. Rev. Lett.* **119**, 127203 (2017).
- [59] S. Ø. Hanslin and A. Qaiumzadeh, Light-induced Dzyaloshinskii-Moriya interactions in antiferromagnetic metals, *Phys. Rev. B* **103**, 134428 (2021).
- [60] I. A. Ado, A. Qaiumzadeh, A. Brataas, and M. Titov, Chiral ferromagnetism beyond Lifshitz invariants, *Phys. Rev. B* **101**, 161403(R) (2020).
- [61] G. Kresse and J. Furthmüller, Efficient iterative schemes for *ab initio* total-energy calculations using a plane-wave basis set, *Phys. Rev. B* **54**, 11169 (1996).
- [62] G. Kresse and J. Furthmüller, Efficiency of *ab-initio* total energy calculations for metals and semiconductors

- using a plane-wave basis set, *Comput. Mater. Sci.* **6**, 15 (1996).
- [63] J. P. Perdew, K. Burke, and M. Ernzerhof, Generalized Gradient Approximation Made Simple, *Phys. Rev. Lett.* **77**, 3865 (1996).
- [64] P. E. Blöchl, Projector augmented-wave method, *Phys. Rev. B* **50**, 17953 (1994).
- [65] G. Kresse and D. Joubert, From ultrasoft pseudopotentials to the projector augmented-wave method, *Phys. Rev. B* **59**, 1758 (1999).
- [66] D. M. Ceperley and B. J. Alder, Ground State of the Electron Gas by a Stochastic Method, *Phys. Rev. Lett.* **45**, 566 (1980).
- [67] J. P. Perdew and A. Zunger, Self-interaction correction to density-functional approximations for many-electron systems, *Phys. Rev. B* **23**, 5048 (1981).
- [68] A. I. Liechtenstein, V. I. Anisimov, and J. Zaanen, Density-functional theory and strong interactions: Orbital ordering in Mott-Hubbard insulators, *Phys. Rev. B* **52**, R5467 (1995).
- [69] T. Ozaki, Variationally optimized atomic orbitals for large-scale electronic structures, *Phys. Rev. B* **67**, 155108 (2003).
- [70] T. Ozaki and H. Kino, Numerical atomic basis orbitals from H to Kr, *Phys. Rev. B* **69**, 195113 (2004).
- [71] T. Ozaki and H. Kino, Efficient projector expansion for the *ab initio* LCAO method, *Phys. Rev. B* **72**, 045121 (2005).
- [72] N. Troullier and J. L. Martins, Efficient pseudopotentials for plane-wave calculations, *Phys. Rev. B* **43**, 1993 (1991).
- [73] OPENMX, <https://www.openmx-square.org>.
- [74] T. Ozaki, Continued fraction representation of the Fermi-Dirac function for large-scale electronic structure calculations, *Phys. Rev. B* **75**, 035123 (2007).
- [75] F. Mahfouzi, G. P. Carman, and N. Kioussis, Magnetoelastic and magnetostrictive properties of Co_2XAl Heusler compounds, *Phys. Rev. B* **102**, 094401 (2020).
- [76] V. M. T. S. Barthem, C. V. Colin, H. Mayaffre, M.-H. Julien, and D. Givord, Revealing the properties of Mn_2Au for antiferromagnetic spintronics, *Nat. Commun.* **4**, 2892 (2013).
- [77] G. Kádár, E. Krén, and M. Márton, New antiferromagnetic intermetallic compound in the Mn-Pd system: MnPd_2 , *J. Phys. Chem. Solids* **33**, 212 (1972).
- [78] A. N. Nateprov, V. Ch. Kravtsov, V. Fritsch, and H. von Löhneysen, Structure and properties of the tetragonal phase of MnCuAs , *Surf. Eng. Appl. Electrochem.* **47**, 540 (2011).
- [79] J. Mündelein and H.-U. Schuster, Preparation and crystal structure of compounds MnCuX ($X=\text{P, As, P}_x\text{As}_{1-x}$), *Z. Naturforsch. B* **47**, 925 (1992).
- [80] H. Zhang and R. Cheng, Magnon thermal Edelstein effect detected by inverse spin Hall effect, *Appl. Phys. Lett.* **117**, 222402 (2020).